compared to synthetic bridgmanites (Fig. 3). As noted above, the holotype specimen of bridgmanite also contains high concentrations of Na. This may extend the stability field of bridgmanite (*25*) and supports charge balance for ferric iron via Na-Fe^{3+}–coupled substitution in holotype bridgmanites at redox conditions below the iron-wüstite buffer (*26*), but plausibly also in the terrestrial and martian (*27*) lower mantles.

The evaluation of the shock conditions in Tenham beyond the examination of plausible recovery paths for bridgmanite is outside the scope of this study. The strict association of akimotoite and bridgmanite and the likely absence of bridgmanite in the matrix of the shock-melt vein are pivotal to an assessment (fig. S3). They suggest that the peak pressure exceeded 23 GPa, with temperatures in the melt exceeding the solidus at ~2200 K. The absence of bridgmanite as isolated crystals within the shock-melt vein suggests that pressures were too low to permit crystallization from melt. Using these constraints, we estimate the conditions of formation of bridgmanite in Tenham to be 23 to 25 GPa and 2200 to 2400 K (fig. S3). This estimate is consistent with a more recent estimate by Xie *et al.* (*20*) based on observation of vitrified bridgmanite. The occurrence of bridgmanite along with conditions of formation of other high-pressure minerals imposes strong constraints on pressure and temperature conditions during high-level shock events in meteorites.

REFERENCES AND NOTES

1. L. Liu, *Geophys. Res. Lett.* **1**, 277–280 (1974).
2. A. E. Ringwood, *Geochim. Cosmochim. Acta* **55**, 2083–2110 (1991).
3. R. J. Hemley, R. E. Cohen, *Annu. Rev. Earth Planet. Sci.* **20**, 553–600 (1992).
4. L. Stixrude, C. Lithgow-Bertelloni, *Annu. Rev. Earth Planet. Sci.* **40**, 569–595 (2012).
5. E. Ito, E. Takahashi, Y. Matsui, *Earth Planet. Sci. Lett.* **67**, 238–248 (1984).
6. E. H. Nickel, J. D. Grice, *Can. Mineral.* **36**, 913–926 (1998).
7. M. Murakami, K. Hirose, N. Sata, Y. Ohishi, *Geophys. Res. Lett.* **32**, L03304 (2005).
8. L. Stixrude, C. Lithgow-Bertelloni, *Geophys. J. Int.* **184**, 1180–1213 (2011).
9. D. J. Durben, G. H. Wolf, *Am. Minerol.* **77**, 890–893 (1992).
10. S. E. Kesson, J. D. Fitz Gerald, *Earth Planet. Sci. Lett.* **111**, 229–240 (1992).
11. F. E. Brenker, T. Stachel, J. W. Harris, *Earth Planet. Sci. Lett.* **198**, 1–9 (2002).
12. R. A. Binns, R. J. Davis, S. J. B. Reed, *Nature* **221**, 943–944 (1969).
13. J. V. Smith, B. Mason, *Science* **168**, 832–833 (1970).
14. G. D. Price, A. Putnis, S. O. Agrell, D. G. W. Smith, *Can. Min.* **21**, 29–35 (1983).
15. N. Tomioka, K. Fujino, *Am. Minerol.* **84**, 267–271 (1999).
16. T. G. Sharp, C. M. Lingemann, C. Dupas, D. Stöffler, *Science* **277**, 352–355 (1997).
17. H. Mori, *J. Minerol. Soc. Japan* **23**, 171–178 (1994).
18. N. Miyajima *et al.*, *Am. Minerol.* **92**, 1545–1549 (2007).
19. M. Miyahara *et al.*, *Proc. Natl. Acad. Sci. U.S.A.* **108**, 5999–6003 (2011).
20. Z. D. Xie, T. G. Sharp, P. S. DeCarli, *Geochim. Cosmochim. Acta* **70**, 504–515 (2006).
21. S.-N. Luo, J. A. Akins, T. J. Ahrens, P. D. Asimow, *J. Geophys. Res.* **109** (B5), B05205 (2004).
22. C. Sanchez-Valle, J. D. Bass, *Earth Planet. Sci. Lett.* **295**, 523–530 (2010).
23. See the supplementary materials.
24. D. R. Hummer, Y. W. Fei, *Am. Minerol.* **97**, 1915–1921 (2012).
25. B. Grocholski, K. Catalli, S.-H. Shim, V. Prakapenka, *Proc. Natl. Acad. Sci. U.S.A.* **109**, 2275–2279 (2012).
26. H. Y. McSween Jr., T. C. Labotka, *Geochim. Cosmochim. Acta* **57**, 1105–1114 (1993).
27. C. M. Bertka, Y. Fei, *J. Geophys. Res.* **102**, 5251–5264 (1997).

ACKNOWLEDGMENTS

The crystallographic information about bridgmanite is available at the Inorganic Crystal Structure Database and American Mineralogist databases and in the supplementary materials. This work was supported by U.S. Department of Energy (DOE) award DESC0005278, NASA grant NNX12AH63G, and NSF grants EAR-1128799, DE-FG02-94ER14466, EAR-0318518, and DMR-0080065. Part of this work was performed at GeoSoilEnviroCARS (Sector 13), Advanced Photon Source, Argonne National Laboratory. GeoSoilEnviroCARS is supported by NSF-EAR-1128799 and DE-FG02-94ER14466). The Advanced Photon Source, a DOE Office of Science User Facility, is operated by Argonne National Laboratory under contract no. DE-AC02-06CH11357. We thank reviewers N. Ross and T. Sharp for their helpful comments.

SUPPLEMENTARY MATERIALS

www.sciencemag.org/content/346/6213/1100/suppl/DC1
Materials and Methods
Figs. S1 to S5
Tables S1 and S2
References (*28*–*66*)
Data Tables S1 and S2

30 July 2014; accepted 22 October 2014
10.1126/science.1259369

CHEMICAL OCEANOGRAPHY

Increasing anthropogenic nitrogen in the North Pacific Ocean

Il-Nam Kim,[1] Kitack Lee,[1]* Nicolas Gruber,[2] David M. Karl,[3] John L. Bullister,[4] Simon Yang,[2] Tae-Wook Kim[5]

The recent increase in anthropogenic emissions of reactive nitrogen from northeastern Asia and the subsequent enhanced deposition over the extensive regions of the North Pacific Ocean (NPO) have led to a detectable increase in the nitrate (N) concentration of the upper ocean. The rate of increase of excess N relative to phosphate (P) was found to be highest (~0.24 micromoles per kilogram per year) in the vicinity of the Asian source continent, with rates decreasing eastward across the NPO, consistent with the magnitude and distribution of atmospheric nitrogen deposition. This anthropogenically driven increase in the N content of the upper NPO may enhance primary production in this N-limited region, potentially leading to a long-term change of the NPO from being N-limited to P-limited.

The rate of deposition of reactive nitrogen (i.e., $NO_y + NH_x$ and dissolved organic forms; see supplementary text S1) from the atmosphere to the open ocean has more than doubled globally over the past 100 years (*1*), reaching a magnitude that is comparable to about half of the global ocean N_2 fixation (*2*). The increase in atmospheric nitrogen deposition (AND) is particularly acute in the North Pacific Ocean (NPO) due to rapid population growth and burgeoning industrial activity in northeast Asian countries. These changes in northeast Asia have markedly increased reactive nitrogen fluxes in the adjacent marine environment (*3*, *4*), largely through atmospheric transport by westerly winds and subsequent deposition. Though it has been recognized that such an increasing addition of reactive nitrogen to the ocean could lead to major changes in the upper ocean nitrogen cycle and biological productivity (*5*), the majority of studies conducted to date have suggested that the impact is small and not detectable (*1*), except in near-shore environments and marginal seas (*3*). A recent study directly comparing nutrient measurements made over more than two decades showed that nitrate (N) concentration has increased in the northeast Asian marginal seas and that this increase was probably due to strongly growing AND (*3*). Here we extend this analysis to the entire NPO and show that the anthropogenic influence has already affected the open-ocean nitrogen cycle.

Owing to a lack of basin-wide, nutrient concentration data of sufficient duration (decades) at strategic locations, we reconstructed the temporal changes in N across the NPO using a method based on the relation between the excess of N in a water parcel relative to that expected based on the phosphate (P) concentration and the chlorofluorocarbon-12 (CFC-12)–derived ventilation age of that water parcel (*6*) (supplementary text S2). The excess in N relative to P—i.e., N^* (*7*, *8*)—at each sampling location was calculated as: $N^* = N - R_{N:P} \times P$, where N and P are the measured concentrations and $R_{N:P}$ is the Redfield ratio of 16:1. Because of increasing

[1]School of Environmental Sciences and Engineering, Pohang University of Science and Technology (POSTECH), Pohang, 790–784, Republic of Korea. [2]Environmental Physics Group, Institute of Biogeochemistry and Pollutant Dynamics, ETH Zürich, Zürich, Switzerland. [3]Daniel K. Inouye Center for Microbial Oceanography, University of Hawaii at Manoa, 1950 East West Road, Honolulu, HI 96822, USA. [4]Pacific Marine Environmental Laboratory, National Oceanic and Atmospheric Administration (NOAA), Seattle, WA 98115, USA. [5]Ocean Circulation and Climate Research Division, Korea Institute of Ocean Science and Technology, Ansan, 426–744, Republic of Korea.
*Corresponding author. E-mail: ktl@postech.ac.kr

Downloaded from www.sciencemag.org on December 11, 2014

biases and uncertainties in the CFC-12–derived ages for water masses >40 years old (*9*), we limited our analysis to water parcels <40 years old (i.e., waters ventilated between the mid-1960s and late-1990s). Although this single–ventilation-age approach has shortcomings compared with methods that estimate the full ventilation-age distribution of a water parcel (*9*), the data used in this study were collected during a period of quasi-linear growth of CFC-12 in the atmosphere (fig. S1 and table S1), and the differences between the two types of tracer-derived ages have little impact on trends examined in the present study (*6*).

Three distinct trends in N^* as a function of depth (or ventilation date) were found in the analysis. Trend 1 shows that if the magnitude of the N sources is similar to that of the N sinks (N sources ≈ N sinks), the seawater N^* values remain approximately unchanged regardless of the age of the water parcels (see the black line in Fig. 1). Trend 1 is typically observed in deep waters (>3000 m) but is not confined to such waters. Trend 1 can also be seen in the upper waters of the Pacific Ocean sector of the Southern Ocean (solid and dotted lines in the upper inset in Fig. 1) and the Indian Ocean (dotted line in the lower inset in Fig. 1), which are regions far removed from major AND sources. Trend 2 shows that if the magnitude of the N sources is less than that of the N sinks (N sources < N sinks), the values of N^* fall below the black line representing trend 1 (see the purple curve and the lower inset in Fig. 1). Trend 2 is applicable to intermediate depths at locations where low O_2 concentrations promote denitrification processes ($NO_3^- \rightarrow N_2O/N_2$), which remove N. If the magnitude of the N sources in recent decades exceeded that of the N sinks (N sources > N sinks), as in trend 3, the values of N^* should increase as the age of a water parcel decreases (see the light blue line in Fig. 1). Trend 3 is usually applicable to the upper ocean, where AND and N_2 fixation overwhelmingly contribute to elevated N^* values (*10*). Thus, to infer the imprint of increasing AND in the NPO, we focus on data exhibiting trend 3.

As mixing of water masses with different initial values of N^* and ventilation age could bias trend 3, we used the extended optimum multiparameter method (supplementary text S3) to separate the temporal N^* trend from any mixing contribution. This analysis was performed along density coordinates σ_θ for the core density layers of the main water masses in all six regions [i.e., region 1: σ_θ = 27.2 to 27.3 for the East Sea Intermediate Water (ESIW), regions 2 to 6: σ_θ = 25.5 to 26.5 for North Pacific Central Water (NPCW)] (insets in Fig. 2, C to H; see also supplementary text S3 and fig. S2). The rate of N^* increase from this isopycnal analysis is in good agreement with the depth-based rates estimated from linear regression of the relation between N^* and the partial pressure of CFC-12 (pCFC-12)–derived ventilation date for data found on trend 3 in all six regions (Fig. 2, B to H, and Table 1). This good consistency indicates that trend 3 is unlikely to be generated by mixing between low-N^* water from low-O_2 intermediate depths and high-N^* upper water. It remains possible that this temporal trend is an artifact arising from the production and remineralization of organic matter occurring at a ratio that is substantially different from our assumed Redfield ratio of 16:1, especially in light of recent findings suggesting that organic matter formed in low latitudes tends to have an N:P ratio substantially above the Redfield ratio (*11*). However, the positive slope of the relation we observed [i.e., decreasing N^* with depth (Fig. 2, B to H)] indicated that this biological process is unimportant, as it would generate the opposite slope in the thermocline. Specifically, the formation of organic matter in the upper ocean with a high N:P ratio would lower N^* values in surface water (*11*) but increase N^* in thermocline waters where the N-rich organic matter is remineralized.

Our mixing-corrected reconstructions of the N^* trends between the late 1970s and mid-1990s show increases at all locations across the NPO (Fig. 2). The rate of N^* increase was highest (~0.24 μmol kg^{-1} yr^{-1}) in the East Sea (region 1 in Fig. 2A) and steadily decreased in an eastward direction with increasing distance from the source continent (Fig. 3). In the East Sea, the N^* values for waters older than 30 years (<1970s) remained constant (N^* = −6.6 ± 0.5 μmol kg^{-1}), whereas the values for waters younger than 30 years (>1970s) increased with time (Fig. 2C). In the mid-latitude NPO (20°N to 40°N), N^* values greater than deep water values began to appear in the upper waters (<600 m) ventilated in the late 1970s (Fig. 2, D to H).

To further confirm that the inferred trends of N^* in the NPO reflect temporal changes in AND and are not mixing artifacts, we analyzed the temporal evolution of N^* in the western and central NPO, where the temporal coverage of the data is sufficient to perform such an analysis. Using the PACIFICA database, we found that in the western and central NPO (upper left inset in Fig. 4A; areas of 20°N to 40°N and 130°E to 180°W), the subsurface N^* (300 to 400 m depth) substantially increased in the past decade (Fig. 4A); the estimated rates within this depth range were comparable to those obtained based on pCFC-12 age (upper right inset in Fig. 4A). This increase in N^* occurred without a concurrent change in dissolved O_2 (fig. S3A) or P (fig. S3B). Similar trends were also observed in the central NPO (i.e., the area between 20°N to 40°N along the 150°W line) (fig. S4). Furthermore, the overall rate of N^* increase (0.04 ± 0.02 μmol kg^{-1} yr^{-1} for the period 1988–2011 for the 100 to 200 m depth interval) observed at Station ALOHA (Hawaii Ocean Time-series) (Fig. 4B) was also comparable to the rate based on pCFC-12 age, although the time frame for the comparison is somewhat different.

To attribute the observed temporal trends in N^* to the recent increases in AND, we need to exclude alternative explanations, in particular the possibility of a recent increase in N_2 fixation. Although we cannot completely exclude this possibility, several lines of evidence indicate that N_2 fixation may not be a major contributor. First, an increase in N_2 fixation would also lead to a decrease in the upper ocean P concentration and a concomitant increase in its thermocline

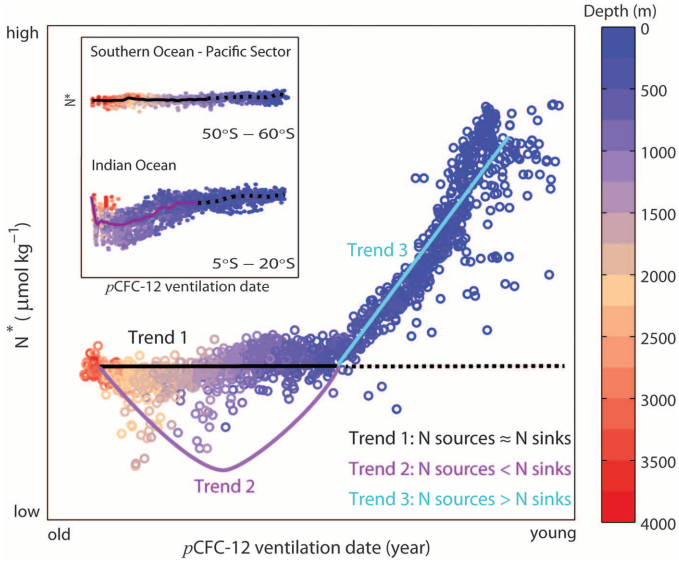


Fig. 1. Three trends of N^* variation. This figure shows the relation between N^* and the pCFC-12–derived ventilation date (which is the year that the CFC-12 concentration in the water sample would have last been in equilibrium with the atmosphere) for seawater samples obtained in the East Sea (Sea of Japan) as part of the Circulation Research of the East Asian Marginal Seas II program in 1999. Trends in the N^* variations associated with three types of cases are presented: Trend line 1 (black solid and dotted lines) indicates a balance of N sources and N sinks, relative to P. Trend line 2 (purple line) would occur if N sinks > N sources (e.g., due to denitrification processes in low-oxygen waters). Trend line 3 (light blue line) indicates major sources of N in recently ventilated waters (and also indicates that N increased over time, regardless of changes in P). The color scale indicates depth. The inset shows the relation between N^* and the pCFC-12–derived ventilation date in the Pacific Ocean sector of the Southern Ocean (50°S to 60°S) and in the tropical Indian Ocean (5°S to 20°S)—two regions far removed from major AND sources—using the PACIFICA and GLODAP databases, respectively.

concentration, which we do not observe (figs. S3 and S4). Second, an increase in N_2 fixation would be expected to shift the peak in the rate of increase of N^* from near the surface to greater depths, as N-rich organic matter of the N_2 fixers is remineralized in the thermocline. In contrast, we observed the highest rate of N^* increase in the surface ocean (Fig. 2). Taken together, these findings suggest that N_2 fixation does not add substantially to the long-term increase in N^* in the NPO. However, some contribution of N_2 fixation cannot be entirely excluded, especially given that the N^*-based rates of N increase exceed the modeled and observed rates of AND (Fig. 3). At region 5 near Hawaii, for example, the N^*-based rates are two to three times higher than the observed rates of AND (from dry and wet deposition). In this region, marine N_2 fixation is estimated to contribute to ~50% of the export production (*12*, *13*).

Having excluded N_2 fixation as a major contributor for most of the NPO, AND remains the only major process that can explain the recent increases in N concentration in the NPO. Several lines of evidence strongly support the conclusion. First, the start of the increase in N^* in the mid-latitude NPO around the 1970s coincided with the onset of a rapid increase in anthropogenic nitrogen emissions from northeast Asian (*14*). Second, the spatial pattern and absolute magnitude of the rate of increase of N^* agreed well with the AND rates derived from an atmospheric transport model (*15*) and observations (*16*, *17*) (Fig. 3). Furthermore, the meridional distribution of aerosol N concentrations was also consistent with the distribution of subsurface N^* in the central NPO (i.e., 200 to 300 m along the 160°E and 180°W lines; see fig. S5). In particular, atmospheric N concentrations measured at Midway (28.2°N and 177.4°W) in the spring (March to

Table 1. Comparison of rates of N^* increase based on isopycnal layer and depth for six regions. See Fig. 2A for region locations. For isopycnal analysis, σ_θ = 27.2 to 27.3, representing the core density layer of ESIW, was chosen for region 1; and σ_θ = 25.5 to 26.5, representing the core density layer of NPCW, was chosen for regions 2 to 6 (fig. S2). Depth rates were derived from Fig. 2.

Regions	Methods	
	Isopycnal	Depth
	(μmol kg^{-1} yr^{-1})	
1	0.24 ± 0.03	0.25 ± 0.01
2	0.11 ± 0.03	0.12 ± 0.01
3	0.11 ± 0.04	0.10 ± 0.03
4	0.04 ± 0.02	0.13 ± 0.02
5	0.03 ± 0.04	0.08 ± 0.01
6	−0.03 ± 0.30	0.03 ± 0.01

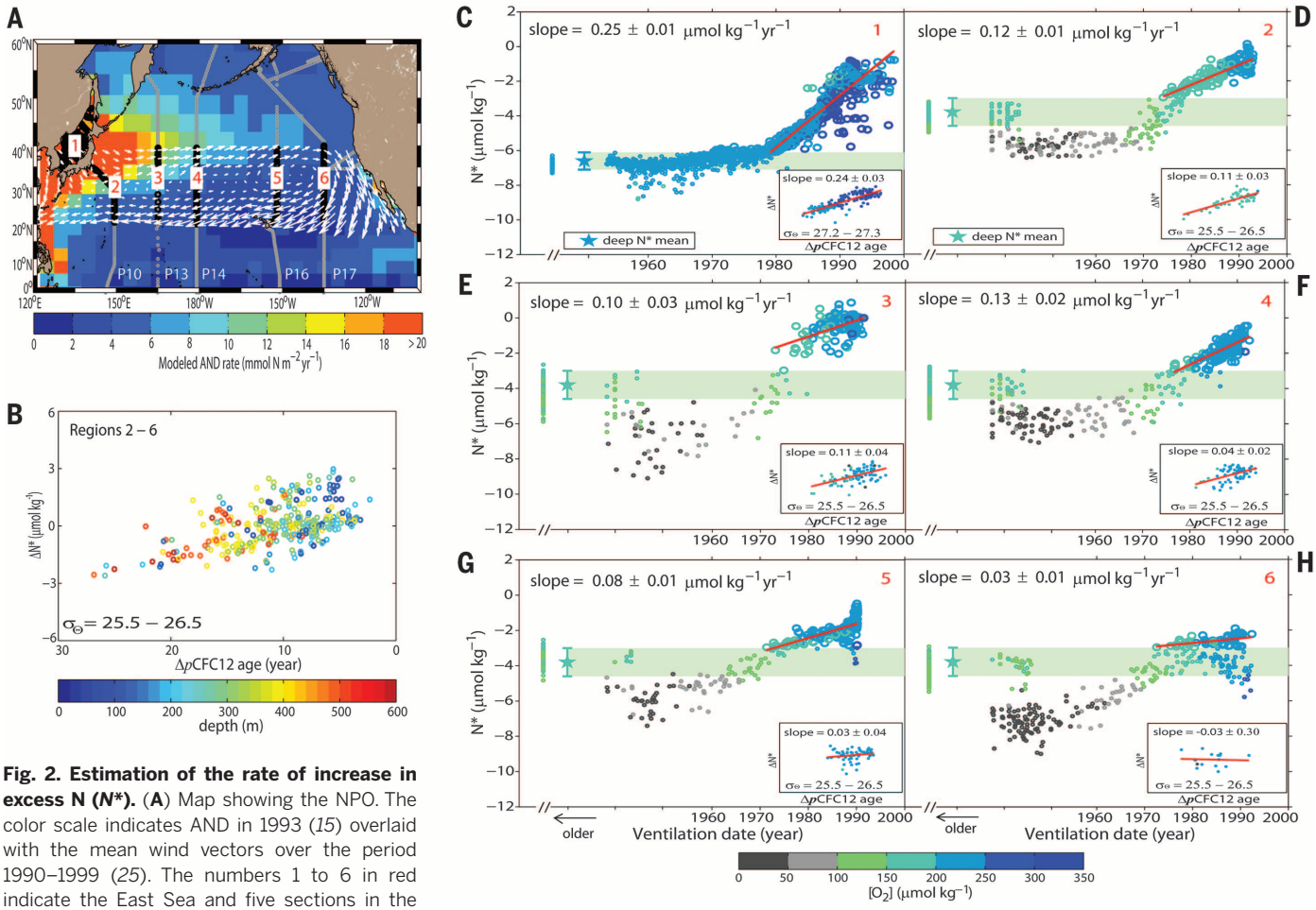


Fig. 2. Estimation of the rate of increase in excess N (N^*). (**A**) Map showing the NPO. The color scale indicates AND in 1993 (*15*) overlaid with the mean wind vectors over the period 1990–1999 (*25*). The numbers 1 to 6 in red indicate the East Sea and five sections in the NPO (P10, P13, P14, P16, and P17), respectively (table S1), and locations of data used in this analysis are shown as black circles. (**B**) Plot of ΔN^* ($\Delta N^* = N^*_{OBS} - \sum x_i N^*_i$) versus ΔpCFC-12 age (ΔpCFC-12 = pCFC-12 age$_{OBS}$ − $\sum x_i p$CFC-12 age$_i$), corrected for the effect of physical mixing (x_i) among different water masses (i.e., Δ = observed value − estimated value from end-member mixing) (*7*), within the range of potential density σ_θ = 25.5 to 26.5 in regions 2 to 6 from the mid-latitude NPO. The color scale indicates water depth. (**C** to **H**) Plots of seawater N^* values (micromoles per kilogram) versus ventilation date (derived from pCFC-12 ages) for regions 1 to 6. Numerical values for ventilation dates are shown only for 1960–2000 due to large uncertainties in earlier dates (see text). The color scale indicates dissolved O_2 concentration. Green shading indicates the envelopes of the deep water N^* values. The star symbols and error bars indicate the mean of the deep water N^* values and the standard deviation (SD) from the mean, respectively. The rates of N^* increase ($N^*_{OBS} > N^*_{DEEP}$) were estimated from the linear regression analysis (shown as the red lines). The insets show plots of seawater ΔN^* versus ΔpCFC-12 age for the core density layers of the ESIW in region 1 (σ_θ = 27.2 to 27.3) and the NPCW in regions 2 to 6 (σ_θ = 25.5 to 26.5). See supplementary text S2 and S3 for the data and isopycnal analysis.

May) showed an increasing trend over the period 1981–2000 (*18*). Third, the magnitude of the AND-induced N^* increase is consistent with expectations based on a simulation conducted with an updated version of the National Center for Atmospheric Research (NCAR) Community Earth System Model (*19*) over the Anthropocene (supplementary text S4 and fig. S6), where AND increased from the pre-industrial era (1850) to modern times (2000). This model includes all of the key processes influencing the marine nitrogen cycle (water-column and benthic denitrification, N_2 fixation, AND, and river inputs) and thus is well suited to analyze the consequences of increasing AND on the ocean nitrogen cycle. Finally, such clear signals of seawater N^* increase are seen only in the NPO and not in comparable mid-latitude Southern Hemisphere sections (fig. S7), where AND has had little impact over the past decades. These observations are also compelling evidence that the observed N^* signals in the NPO are due to the effect of AND. Thus, the balance of evidence suggests that the observed increase in N^* in the upper NPO is a consequence of the recent increase in AND, resulting largely from the dramatic increase in anthropogenic nitrogen emissions in northeastern Asia.

The possible impacts of this anthropogenic perturbation on the open-ocean nitrogen cycle are numerous. The NPO is generally thought to be N-limited (*2*, *13*); therefore, the input of nitrogen may increase primary and export production. In the mid-latitude NPO, the rate of N increase is equivalent to 10 ± 2% (*20*) of the export production (~1.5×10^3 mmol C m^{-2} yr^{-1}) (*21*), which is comparable to the rate derived from AND modeling (*5*). Given the likelihood that the magnitude of AND will continue to increase in the future (*22*), the mid-latitude NPO could rapidly switch to having surplus N. Thus, past and future increases in AND have the potential to alter the phytoplankton community composition and, in

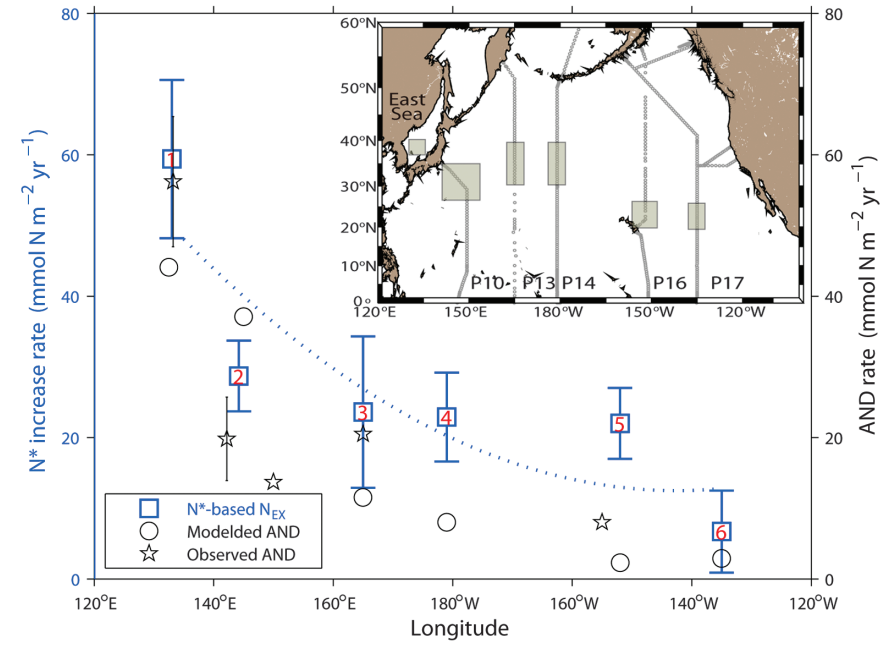
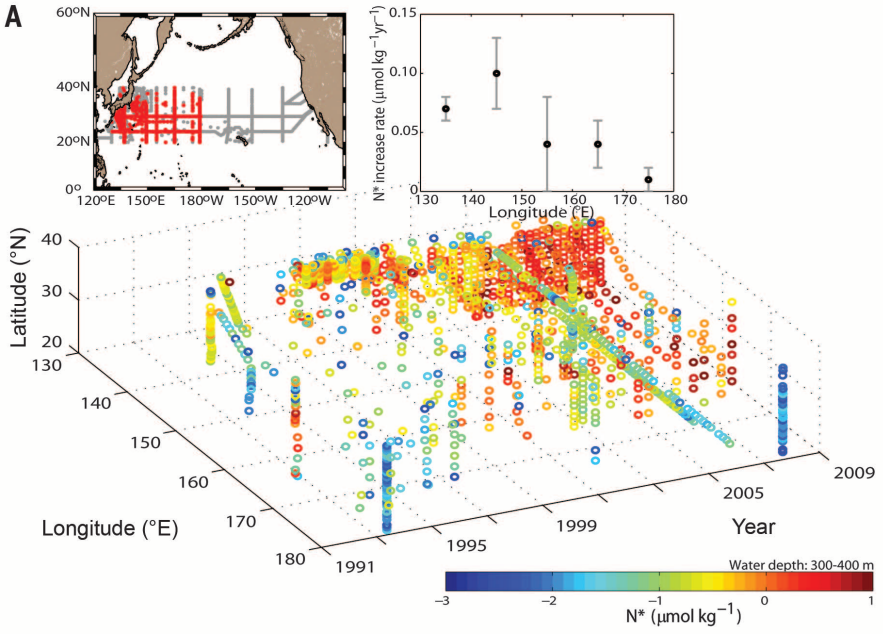


Fig. 3. Comparison of the *N-based rates with AND rates.** Comparison of the N^* values integrated over the water column [$\int_0^z N^*/p\mathrm{CFC}-12\ \mathrm{age}\ dz$, where z is the depth at which the N^* ($N^*_{OBS} > N^*_{DEEP}$) signal was observed, blue squares] with the modeled (circles) (*15*) and observed (stars) (*16*, *17*) AND rates (see supplementary text S5 for the AND rates observed in the mid-latitude NPO). The blue dotted line indicates a least-squares curve fitting of the N^*-based rates. The inset shows the locations (shaded boxes) at which the experimental seawater N^* increase rates were compared with the modeled and observed AND rates. Error bars indicate the SD from the mean.



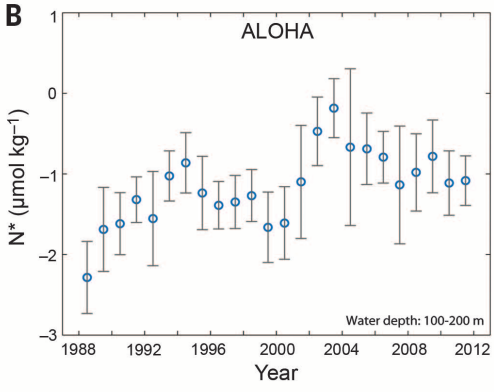


Fig. 4. Temporal variations of *N.** (**A**) Distribution of N^* in the western and central NPO (20°N to 40°N and 130°E to 180°W) determined from data in the PACIFICA database collected between 300 and 400 m in the period 1992–2008. The upper left inset shows the data points (red) used in this analysis. The upper right inset shows the rates of N^* increase averaged for each 10° longitude interval. Note that the midpoints in the inset (upper right) are plotted on the x axis. The error bars in the inset (upper right) indicate the SD from the mean. (**B**) Rate of N^* increase estimated from the annual mean N^* (averaged between 100 and 200 m) over the period 1988–2011 at Station ALOHA (see supplementary text S2 for the ALOHA nutrient data). Error bars indicate the SD from the mean. The rate of N^* increase is 0.04 ± 0.02 μmol kg^{-1} yr^{-1}, as was estimated from a least-squares linear regression of data obtained during the period 1988–2011.

the long term, the structure of the ecosystem. In addition, such anthropogenic nitrogen inputs into the NPO could also enhance N_2O production due to an increase in remineralization in association with enhanced export production levels and potentially stimulate denitrification (*1*, *23*). If similar trends are confirmed across the other major ocean basins, it would constitute another example of a global-scale alteration of the Earth system.

REFERENCES AND NOTES

1. R. A. Duce *et al.*, *Science* **320**, 893–897 (2008).
2. N. Gruber, in *Nitrogen in the Marine Environment, The Marine Nitrogen Cycle: Overview and Challenges*, D. G. Capone, D. A. Bronk, M. R. Mulholland, E. J. Carpenter, Eds. (Elsevier, Amsterdam, 2008), pp. 1–50.
3. T.-W. Kim, K. Lee, R. G. Najjar, H.-D. Jeong, H. J. Jeong, *Science* **334**, 505–509 (2011).
4. J. N. Galloway, *Nutr. Cycl. Agroecosyst.* **57**, 1–12 (2000).
5. G. S. Okin *et al.*, *Global Biogeochem. Cycles* **25**, GB2022 (2011).
6. S. C. Doney, J. L. Bullister, *Deep-Sea Res. A* **39**, 1857–1883 (1992).
7. N. Gruber, J. L. Sarmiento, *Global Biogeochem. Cycles* **11**, 235–266 (1997).
8. A. F. Michaels *et al.*, *Biogeochemistry* **35**, 181–226 (1996).
9. R. A. Fine, *Annu. Rev. Mar. Sci.* **3**, 173–195 (2011).
10. A. Singh, M. W. Lomas, N. R. Bates, *Deep-Sea Res. II* **93**, 148–158 (2013).
11. A. C. Martiny *et al.*, *Nat. Geosci.* **6**, 279–283 (2013).
12. K. Lee, *Limnol. Oceanogr.* **46**, 1287–1297 (2001).
13. D. Karl *et al.*, *Nature* **388**, 533–538 (1997).
14. H. Akimoto, H. Narita, *Atmos. Environ.* **28**, 213–225 (1994).
15. F. J. Dentener, Global maps of atmospheric nitrogen deposition, 1860, 1993, and 2050. Data set (Oak Ridge National Laboratory Distributed Active Archive Center, Oak Ridge, TN, 2006); http://daac.ornl.gov/.
16. J. Jung, H. Furutani, M. Uematsu, *J. Atmos. Chem.* **68**, 157–181 (2011).
17. J. H. Carrillo, M. G. Hastings, D. M. Sigman, B. J. Huebert, *Global Biogeochem. Cycles* **16**, 1076 (2002).
18. J. M. Prospero, D. L. Savoie, R. Arimoto, *J. Geophys. Res.* **108**, 4019 (2003).
19. J. K. Moore, K. Lindsay, S. C. Doney, M. C. Long, K. Misumi, *J. Clim.* **26**, 9291–9312 (2013).
20. The 2% error is 1 SD from the mean export production estimated using the rate of seawater N^* increase found in regions 2 to 5 shown in Fig. 3.
21. K. Lee, D. M. Karl, R. Wanninkhof, J.-Z. Zhang, *Geophys. Res. Lett.* **29**, 1907 (2002).
22. Future projections suggest that AND in 2030 may be up to 30% higher than in 2000 in the mid-latitude NPO (*1*). In particular, NH_x deposition in 2100 may be double that in 2000 (*24*), whereas NO_y deposition is likely to decrease substantially due to regulation of emissions. This perturbation, in conjunction with enhanced ocean stratification, could become a key factor determining future primary and export production in the NPO.
23. P. Suntharalingam *et al.*, *Geophys. Res. Lett.* **39**, L07605 (2012).
24. P. Ciais *et al.*, in *Climate Change 2013: The Physical Science Basis, Contribution of Working Group I to the Fifth Assessment Report of the Intergovernmental Panel on Climate Change*, T. F. Stocker *et al.*, Eds. (Cambridge Univ. Press, Cambridge, 2013), chap. 6.
25. Mean wind data during 1990–1999 are available at www.esrl.noaa.gov/psd/.

ACKNOWLEDGMENTS

We thank all scientists responsible for the CFC-12 and nutrient measurements in the GLODAP (http://cdiac.ornl.gov/oceans/glodap/) and PACIFICA (http://cdiac.ornl.gov/oceans/PACIFICA/) databases and the CREAMS II (http://sam.ucsd.edu) and HOT (http://hahana.soest.hawaii.edu/hot/) programs. This research was supported by the Mid-Career Researcher Program (no. 2012R1A2A1A01004631) and the Global Research Project funded by the National Research Foundation (NRF) of Ministry of Science, Information Communication Technology, and Future Planning, Science and Technology (no. 2013K1A1A2A02078278). Partial support was provided by the "Management of marine organisms causing ecological disturbance and harmful effects" program funded by the Ministry of Oceans and Fisheries. T.-W.K. was supported by the Basic Science Research Program through NRF (no. 2012R1A6A3A0403883). D.M.K was funded by the NSF (nos. OCE09-26766 and EF04-24599) and the Gordon and Betty Moore Foundation. J.L.B. was funded by NOAA's Climate Program Office. N.G. and S.Y. acknowledge the financial support from ETH Zürich. Author contributions: I.-N.K. and K.L. designed the study and wrote the manuscript with support from N.G., D.M.K., and J.L.B. I.-N.K. analyzed the data. N.G., D.M.K., J.L.B., S.Y., and T.-W.K. contributed to the manuscript with discussions and comments. S.Y. and N.G. performed NCAR Community Earth System Model simulations. The authors declare no competing financial interests.

SUPPLEMENTARY MATERIALS

www.sciencemag.org/content/346/6213/1102/suppl/DC1
Supplementary Text
Figs. S1 to S7
Tables S1 and S2
References (*26*–*33*)

7 July 2014; accepted 3 November 2014
10.1126/science.1258396

COGNITIVE PSYCHOLOGY

Forgetting the presidents

H. L. Roediger III* and K. A. DeSoto

Two studies examined how U.S. presidents are forgotten. A total of 415 undergraduates in 1974, 1991, and 2009 recalled as many presidents as possible and attempted to place them in their correct ordinal positions. All showed roughly linear forgetting of the eight or nine presidents prior to the president holding office at the time, and recall of presidents without respect to ordinal position also showed a regular pattern of forgetting. Similar outcomes occurred with 497 adults (ages 18 to 69) tested in 2014. We fit forgetting functions to the data to predict when six relatively recent presidents will recede in memory to the level of most middle presidents (e.g., we predict that Truman will be forgotten to the same extent as McKinley by about 2040). These studies show that forgetting from collective memory can be studied empirically, as with forgetting in other forms of memory.

The name of the president of the United States is known to virtually all adult Americans. When doctors wish to test the cognitive status of a concussion or stroke patient, they often ask the patient to identify the current president; a response of "Ronald Reagan" in 2014, for example, reveals a probable deficit. Once they leave office, however, presidents recede from the memory of U.S. citizens. For instance, today presidents such as Fillmore, Pierce, and Arthur are barely remembered at all, yet at one point in America's past their names were known by all U.S. adults, just as the names Obama or Bush are known in 2014.

The purpose of this project was to study how presidents are forgotten from collective memory. Collective memory, sometimes called historical or popular memory, refers to the representation of the past shared by a group (*1*–*4*). Most studies in this tradition focus on how events of historical significance are remembered (e.g., the Holocaust, the 9/11 attacks), whereas our focus is on historical forgetting [see (*5*)].

We can assume that recall of a president is 100% while the president holds office and begins to drop when he leaves office. Our question is: What is the rate at which samples of U.S. citizens forget the presidents over time?

Across two studies, we determined the rate at which presidents recede from collective memory of (i) college students and (ii) a wider sample of Americans (taken from Amazon Mechanical Turk; MTurk). We measured memory for each president using both ordinal position recall and free recall criteria. Ordinal position recall describes whether an individual can place a president in the ordinal position in which he served (e.g., Lincoln in position 16). Free recall assesses whether an individual can recall a president's name at all, regardless of ordinal position. To measure forgetting, we applied two methods to the resulting sets of data. We examined the decline in recall within each group of subjects from the current president at the time of testing to the next most recent and so on (i.e., the recency effect in recall within groups of individuals). In the second method, we computed forgetting curves for six presidents across three generations of college students.

In our first study, we tested three generations of college undergraduates in three widely separated years: 159 subjects in 1974 (*6*), 106 in 1991 (*7*), and 150 in 2009. In each case the students were given a sheet of paper numbered according to the number of presidents (e.g., numbers 1 through 41 in 1991), with instructions to try to recall as many presidents as possible and to place them in their correct ordinal position. Students were told that if they recalled a president but not his ordinal position, they should guess or simply list that president off to the side of the page. They were given 5 min for recall, which prior research has shown is sufficient time to exhaust students' knowledge (*8*). Figure 1A shows recall of presidents as a function of their chronological term in office, when students were given credit for

Department of Psychology, Washington University, St. Louis, MO 63130, USA.
*Corresponding author. E-mail: roediger@wustl.edu

www.sciencemag.org/content/346/6213/1102/suppl/DC1

Supplementary Materials for

Increasing anthropogenic nitrogen in the North Pacific Ocean

Il-Nam Kim, Kitack Lee,* Nicolas Gruber, David M. Karl, John L. Bullister, Simon Yang, Tae-Wook Kim

*Corresponding author. E-mail: ktl@postech.ac.kr

Published 28 November 2014, *Science* **346**, 1102 (2014)
DOI: 10.1126/science.1258396

This PDF file includes:

Supplementary Text
Figs. S1 to S7
Tables S1 and S2
Full Reference List

Supplementary Text

S1. Atmospheric reactive nitrogen species and ocean excess N

Atmospheric emissions of reactive nitrogen are largely in the form of oxidized or reduced nitrogen species (NO_y and NH_x) produced as byproducts of fossil fuel combustion and from the use of fertilizers in agriculture, respectively. Atmospheric deposition of soluble organic nitrogen can also give rise to a portion of the reactive nitrogen pool (*26*), especially in surface waters in selected regions. However, the contribution of dissolved organic nitrogen to total reactive nitrogen is difficult to estimate because of a lack of field measurements. Therefore, our N^* ($= N - R_{N:P} \times P$) (*7, 8*) calculation did not include dissolved organic nitrogen.

Our N^* calculation probably included NH_4^+ because a substantial fraction of NH_4^+ deposited into seawater is ultimately transformed into NO_3^- (*2*). The NH_4^+ in the euphotic layer that is not nitrified is rapidly assimilated into organic matter, and eventually remineralized in the upper thermocline, just below the euphotic layer. All of the NO_3^- formed by remineralization in the upper thermocline is likely to be mixed back into the euphotic layer on time scales less than one year.

S2. Ocean data (nutrients and CFC-12) used

Multi-national and multi-agency efforts yielded the high quality hydrographic, nutrient, and CFC-12 data sets used in this study. Data from the East Sea were collected by teams from three countries, the USA, South Korea, and Russia as part of the Circulation Research of the East Asian Marginal Seas II (CREAMS II) (Table S1). Most of the data from the locations (i.e. the P10, P13, P14, P16, and P17 lines) in the North Pacific Ocean (NPO) were collected as part of the World Ocean Circulation Experiment (WOCE) by teams from the USA (Table S1). We used only those data with concentrations greater than 0.1 μmol kg^{-1} for N and 0.01 μmol kg^{-1} for P, which are the approximate analytical detection limits of N and P for the methods employed in these field studies (*27*). The data used in this study are available at http://cdiac.ornl.gov/oceans/glodap/ (GLODAP database), http://sam.ucsd.edu (CREAMS II database), and http://cdiac.ornl.gov/oceans/ PACIFICA/ (PACIFICA database). In Fig. 4b, we used nutrient data (nitrate + nitrite and P data between 100 m and 200 m depth measured by auto-analyzer) observed at station ALOHA through the Hawaii Ocean Time-series (HOT) program (data available at http://hahana.soest.hawaii.edu/hot/).

The CFC-12 derived ventilation age of a water parcel collected at time t was calculated by first converting the measured CFC-12 concentration (in picomoles kg^{-1}) to its partial pressure (pCFC-12), based on the sample's potential temperature and salinity. The pCFC-12 value was then matched to the atmospheric growth record for CFC-12 to determine the calendar year (τ) in which the CFC concentration in the water sample would have been in equilibrium with the atmosphere (i.e. the 'ventilation date') (*6*). Thus, the pCFC-12 age or 'ventilation age' of a water parcel is given as $t - \tau$.

The effect of the timing of sampling on our analysis can be evaluated using the following two cases. Case 1: sampling is done in different seasons. The concentrations of individual nutrients (N and P) vary considerably across seasons (i.e. low in summer and high in winter). However, N^* values (the key parameter used in our analysis) tend to be largely insensitive to the seasons because the major drivers for seasonal N and P change (biological uptake and release of N and P; entrainment of deep water) affect the concentrations of N and P in near Redfield ratio and thus do not change N^* values considerably. Case 2: sampling

occurs several years apart. Under this scenario, the obtained datasets would have different N^* values because the upper waters of the NPO would receive increasing amounts of N over time due to increases in atmospheric nitrogen deposition (AND). Such temporal variations in N^* in the upper NPO are what we are trying to elucidate from nutrient data. To do so we determined the age of an individual water mass (the time elapsed since the water mass lost contact with the atmosphere) in the upper NPO and its intrinsic N^* value imprinted when the water mass left the surface. Therefore, the difference in the timing of sampling (different seasons and years) did not result in biases in our analysis (N^* versus the age of the water mass).

S3. Isopycnal analysis

The rate of N^* increase was calculated based on the relationship between ΔN^* and ΔpCFC-12 age along the core density layers (σ_θ = 27.2–27.3 for East Sea Intermediate Water in region 1 and σ_θ = 25.5–26.5 for North Pacific Central Water in regions 2–6) (*28, 29*), after correcting for biases arising from mixing of water masses in the following manner (*7*):

$$\sum x_i = 1 \tag{S1}$$

$$N^*_{OBS} = \sum x_i \cdot N^*_i + \Delta N^* \tag{S2}$$

$$p\text{CFC-12 age}_{OBS} = \sum x_i \cdot p\text{CFC-12 age}_i + \Delta p\text{CFC-12 age} \tag{S3}$$

where x is the water mass fraction, N^*_{OBS} indicates observed N^*, and the subscript i indicates water masses involved in mixing. To estimate the mixing fractions of water masses identified in the core density layers we used the extended Optimum Multi-parameter (eOMP) analysis (*30*) (further details can be found at http://omp.geomar.de/). In the East Sea (region 1 in Fig. 2a) three water masses including the Tsushima Middle Water (TMW), the East Sea Intermediate Water (ESIW), and the East Sea Proper Water (ESPW) were involved in mixing (*28*), whereas in the NPO (regions 2–6), three water masses including the upper North Pacific Central Water (NPCW), the lower NPCW, and the California Current System Water (CCSW) (*29*) were involved in mixing. The parameters used in the eOMP analysis include potential temperature (PT), salinity (S), dissolved oxygen (Oxy), nitrate (N), phosphate (P) and silicate (Si). The eOMP analysis takes the following matrix form:

$$\begin{bmatrix} PT_1 & + & \cdots & + & PT_i & + & 0 \\ S_1 & + & \cdots & + & S_i & + & 0 \\ Oxy_1 & + & \cdots & + & Oxy_i & - & r_{O2/P} \\ P_1 & + & \cdots & + & P_i & + & 1 \\ N_1 & + & \cdots & + & N_i & + & r_{N/P} \\ Si_1 & + & \cdots & + & Si_i & + & r_{Si/P} \\ 1 & + & \cdots & + & 1 & + & 0 \end{bmatrix} \times \begin{bmatrix} x_1 \\ \vdots \\ x_i \\ \Delta P_{remi} \end{bmatrix} - \begin{bmatrix} PT_{obs} \\ S_{obs} \\ Oxy_{obs} \\ P_{obs} \\ N_{obs} \\ Si_{obs} \\ 1 \end{bmatrix} = \begin{bmatrix} R_{PT} \\ R_S \\ R_{Oxy} \\ R_P \\ R_N \\ R_{Si} \\ R_{MC} \end{bmatrix} \tag{S4}$$

$$\boldsymbol{A} \cdot \boldsymbol{X} - \boldsymbol{b} = \boldsymbol{R}$$

where the matrix $\boldsymbol{A}$ is defined as the properties of the predefined end-members ($i \leq 5$), the column vector $\boldsymbol{X}$ is composed of physical mixing fractions (x_i) among the end-members and the amount of remineralized phosphate (ΔP_{remi}), the column vector $\boldsymbol{b}$ is the observations, and

the column vector ***R*** represents the residuals of parameters. The last row that consists of '1' is the mass conservation ($\sum x_i = 1$). The ratios of $r_{Si:N:P:-O2}$ stand for the Redfield ratios. The eOMP analysis was based on an over-determined system, so the solutions (***X***) were found by minimizing non-negative residuals (*30*). The residuals for mass conservation, which is a tracer to determine the validity of the result of the eOMP analysis (*31*), were defined within ~5%. The physicochemical characteristics of end-members used for the isopycnal analysis are summarized in Table S2.

S4. Model simulation for $\Delta N^*_{2000-1850}$

To simulate $\Delta N^*_{2000-1850}$ ($= N^*_{2000} - N^*_{1850}$) derived from the effect of AND, we used the most recent version of the NCAR Community Earth System Model, which includes fully interactive nitrogen processes (i.e. water-column and benthic denitrification, marine N_2 fixation, AND, and river inputs) (*19*). The model was initially run for more than 1000 years in order to approach an equilibrium state. The pre-industrial rate of AND onto the ocean was ~7 Tg N yr^{-1}. Our simulations began in 1850 and was run until 2000, based on the history of AND (*32*). In 2000, the amount of AND was ~56 Tg N yr^{-1}.

S5. The observed AND rates in the mid-latitude NPO

In Fig. 3, for comparison with N^*-based and modeled estimates, we used the mean AND rates observed at Oki (36.3°N and 133.2°E, over the period 2002–2008) and Ogasawara (27.1°N and 142.2°E, over the period 2000–2009), both of which were obtained by the Acid Deposition Monitoring Network in East Asia (EANET) (at http: //www.eanet.asia/). Shipboard measurements (Aug.–Sep. 2008 and Jan. 2009) (*16*) from the western (30°N–35°N and 145°E–155°E) and the central NPO (30°N–35°N and 160°E–170°E) and measurements at Hawaii (19.4°N and 155.0°W) over the period 1993–2000 (*17*) were also used for comparison. The rates of N^* increase and of the modeled AND were derived from locations nearest to the sites where observations were available (the shaded boxes in the inset). Note that the values of Jung et al. (2011) collected from the region between 20°N and 40°N (*16*) were only used in this and not in any other analysis.

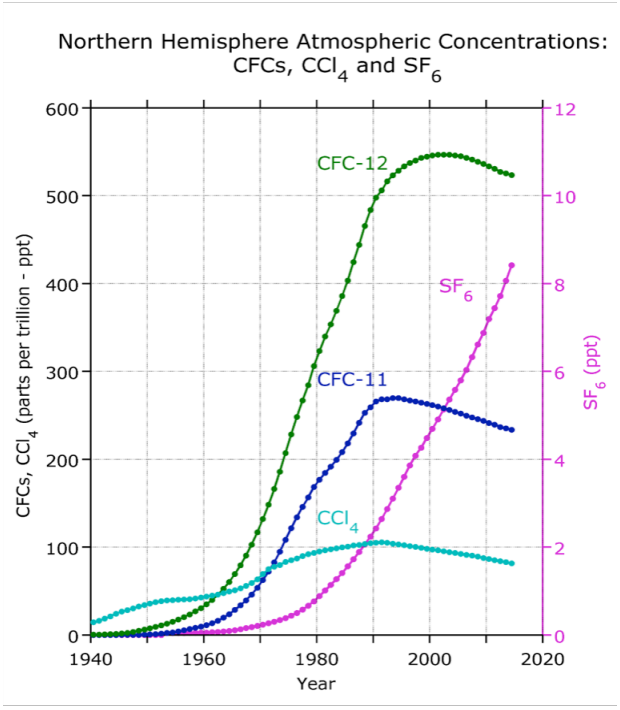


Fig. S1.

Evolution of the atmospheric concentrations of CFC-11, CFC-12, CCl_4, and SF_6 in the northern hemisphere (plotted using data obtained from http://cdiac.ornl.gov/oceans/new_atmCFC. html).

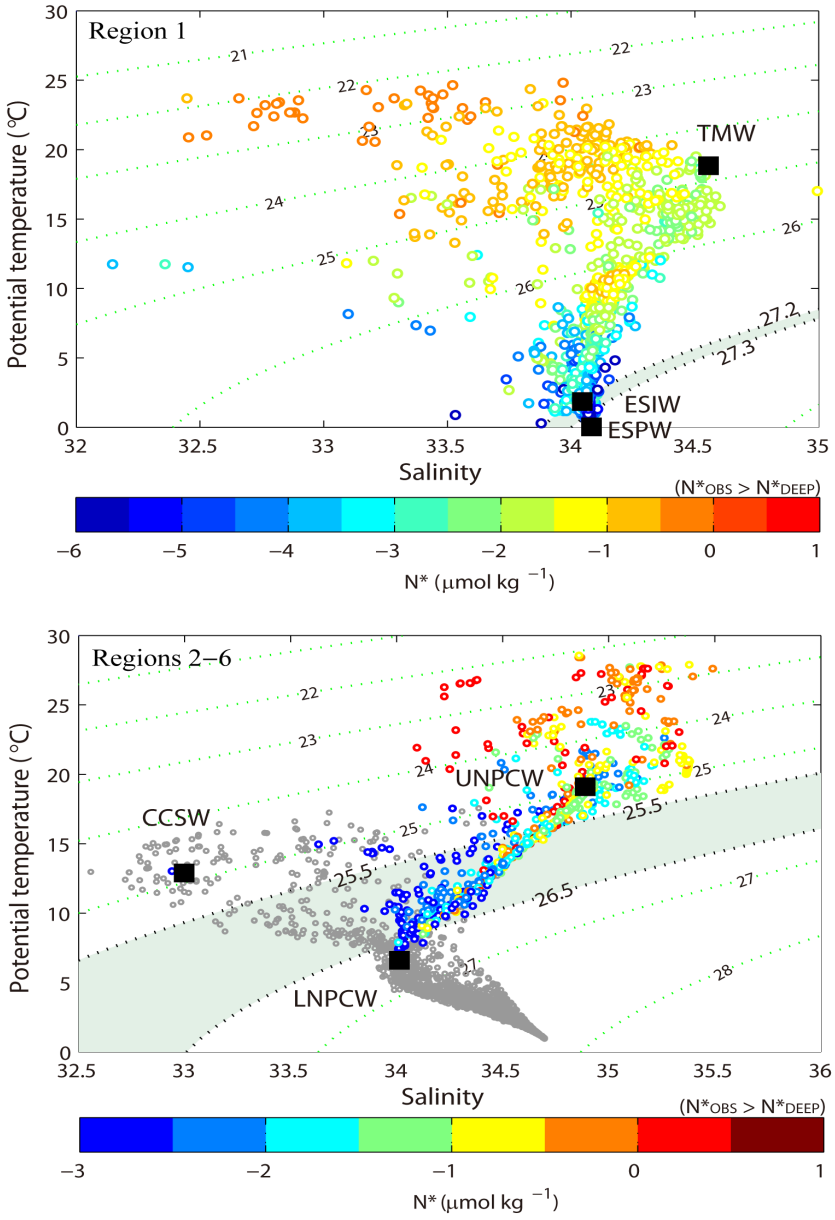


Fig. S2.

Indicative potential temperature and salinity diagram for the East Sea (data from region 1 in Fig. 2a) and the NPO (data from regions 2–6 in Fig. 2a). Color scales indicate N^* ($N^*_{OBS} > N^*_{DEEP}$) in the upper waters. The isopycnal analysis was performed on the density layer σ_θ = 27.2–27.3 (the shaded) for the East Sea and on the density layer σ_θ = 25.5–26.5 for the NPO (Figs. 2c–h and Table 1). The Tsushima Middle Water (TMW), East Sea Intermediate Water (ESIW), and East Sea Proper Water (ESPW) were involved in mixing in the East Sea (region 1). The California Current System Water (CCSW) and Upper/Lower North Pacific Central Water (U/LNPCW) were involved in mixing in the NPO (regions 2–6).

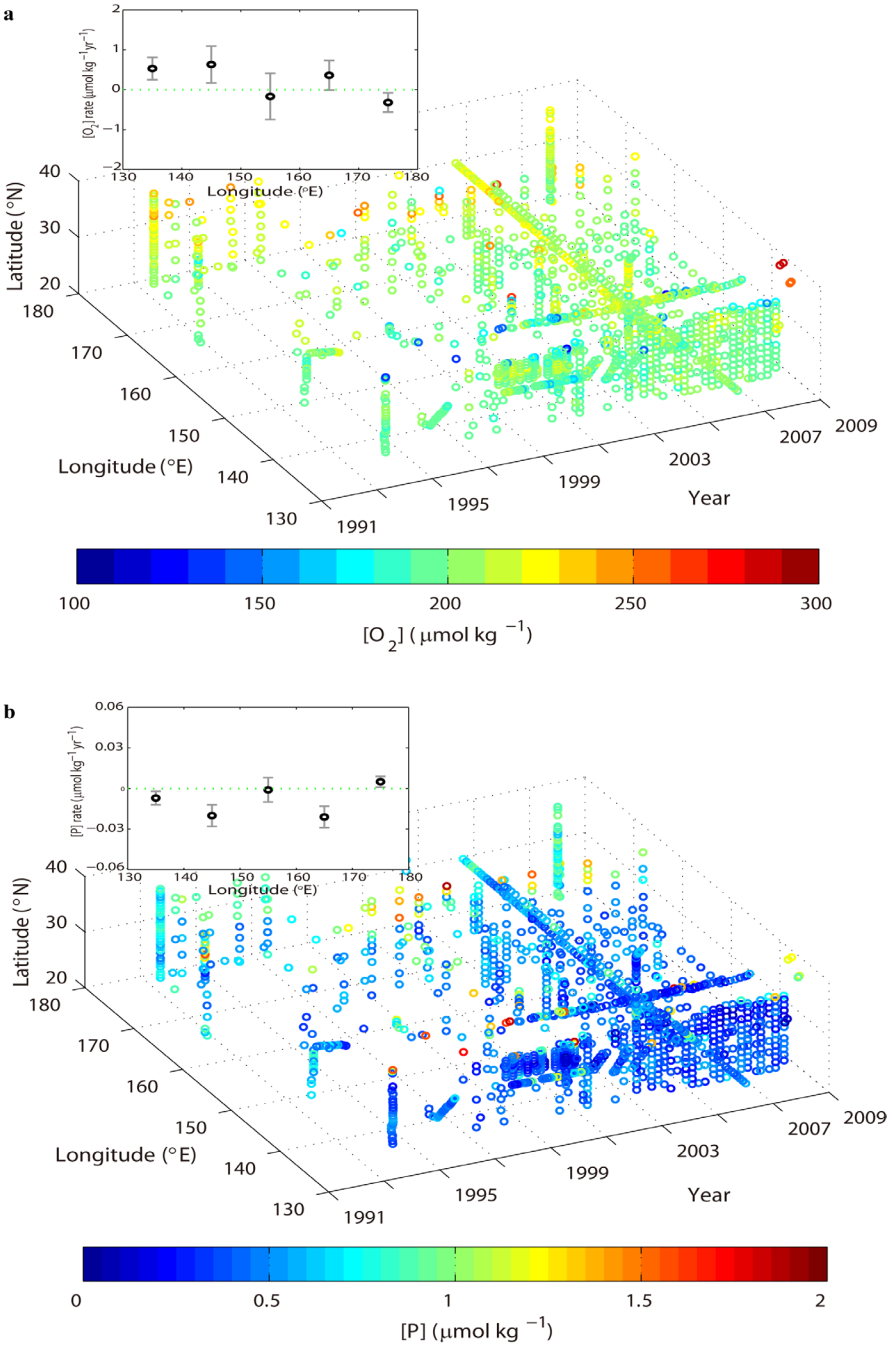


Fig. S3

Distributions of **a.** dissolved O_2 ([O_2]) and **b.** phosphate concentrations ([P]) in the western and central NPO (20°N–40°N and 130°E–180°E) determined from data in the PACIFICA database collected between 300 m and 400 m in a period 1992–2008. The insets (**a** and **b**) show the rates of [O_2] and [P] averaged for each 10° longitude interval, respectively. Note that the mid-points in the insets are plotted on the x-axis, and the error bars in the inset indicate the standard deviation from the mean.

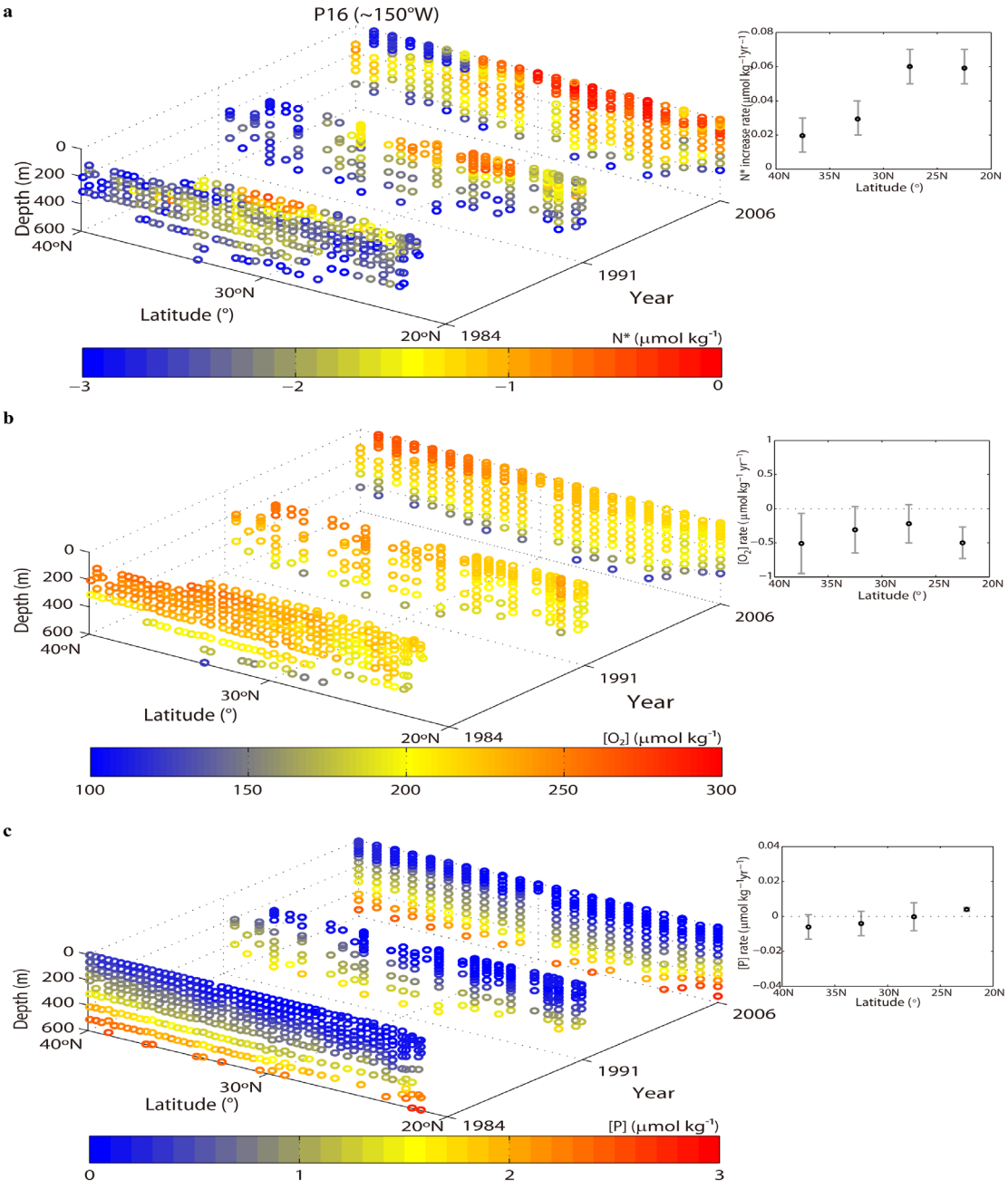


Fig. S4

Meridional distributions of **a.** N^* ($N^*_{OBS} > N^*_{DEEP}$), **b.** dissolved O_2 concentrations ($[O_2]$), and **c.** phosphate concentrations ([P]) in the upper layer (< 600 m) along the P16 line (~150°W), from data collected in 1984, 1991, and 2006. The inset shows the rates of N^*, $[O_2]$, and [P] averaged for each 5° latitude interval. Note that the mid-points in the insets are plotted on the x-axis. The error bars in the inset indicate the standard deviation from the mean.

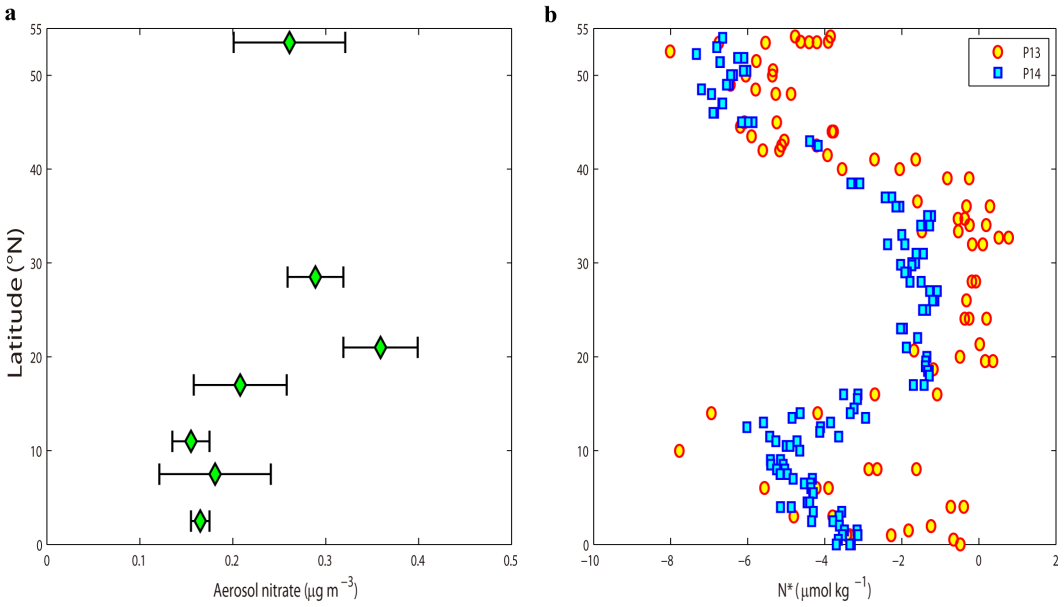


Fig. S5

Meridional distributions of **a.** the aerosol nitrate concentrations (diamonds) and **b.** the subsurface N^* values (200–300 m in the P13 and P14 lines) in the central NPO. The error bars in **a.** represent standard deviations from the mean. The symbols of circles and squares in **b.** indicate data obtained from the P13 and P14 lines, respectively. The aerosol nitrate concentrations were reproduced from Prospero and Savoie (1989) (*33*).

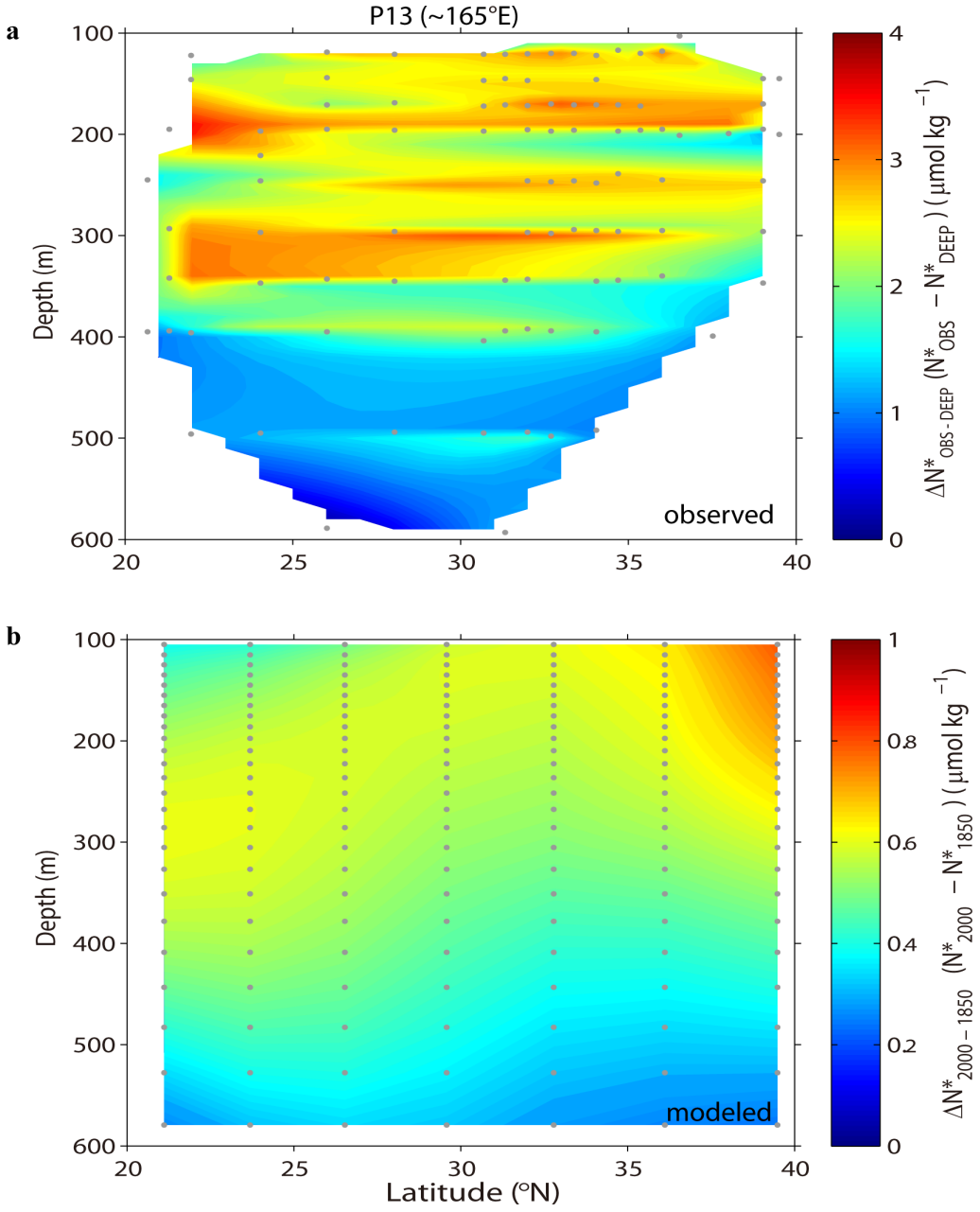


Fig. S6

Comparison of the distribution of **a.** observed $\Delta N^*_{OBS-DEEP}$ values relative to deep ocean values ($= N^*_{OBS} - N^*_{DEEP}$, when $N^*_{OBS} > N^*_{DEEP}$) in WOCE section P13 (~165°E) with **b.** the simulated $\Delta N^*_{2000-1850}$ ($= N^*_{2000} - N^*_{1850}$) values from the recent NCAR Community Earth System Model with fully interactive nitrogen processes (see supplementary text S4).

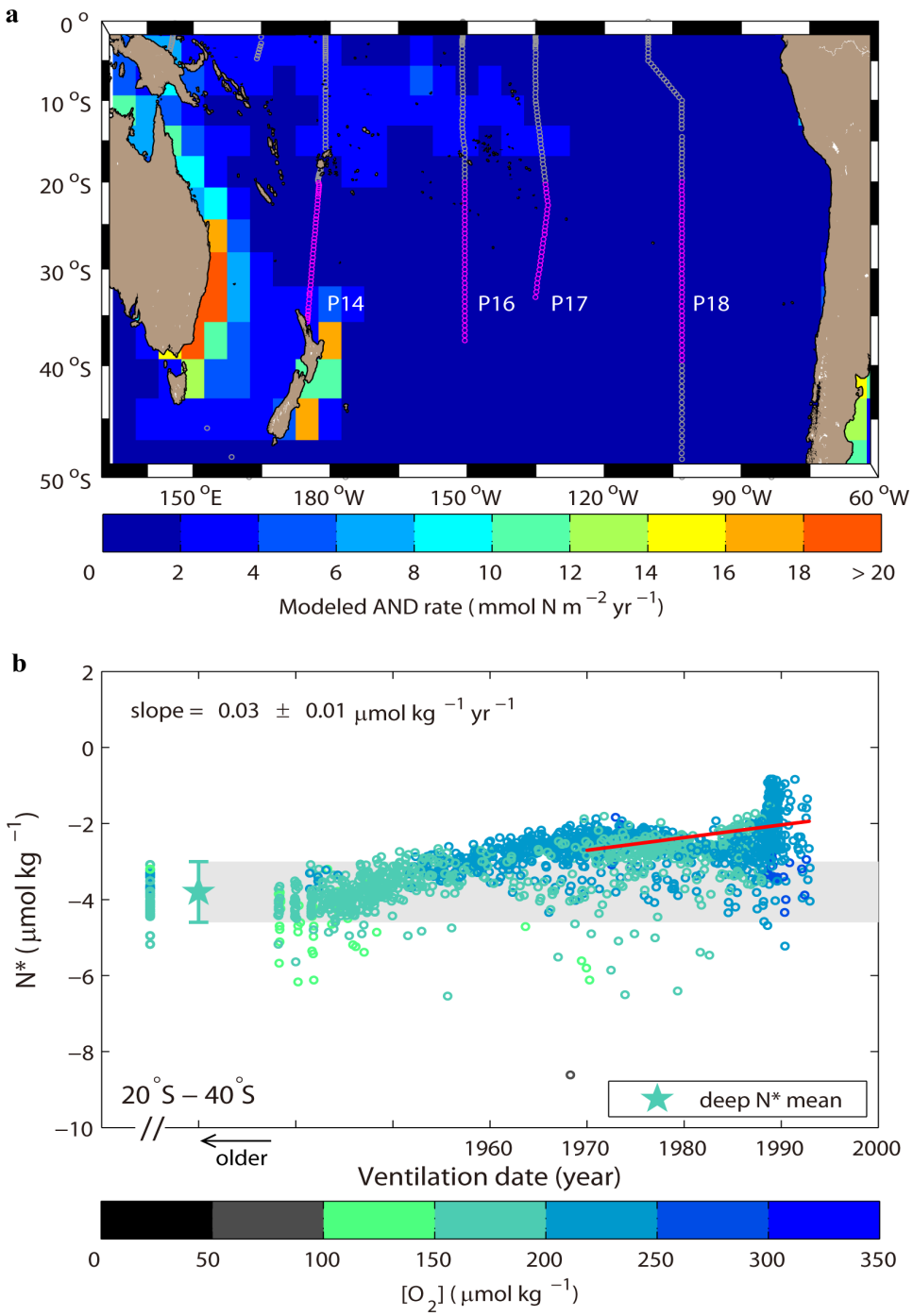


Fig. S7

a. A map showing the data points (pink circles) used for this analysis. **b.** Estimation of the rate of N^* ($N^*_{OBS} > N^*_{DEEP}$) increase using the relationship between N^* and *p*CFC-12 derived ventilation date in the mid-latitude South Pacific Ocean (20°S–40°S). The color scales indicate the dissolved O_2 concentrations.

185 **Table S1.**

186 Summary of cruise data (N, P, [O_2], and [CFC-12]) used in this study. Note that the data used
187 in Fig. 4a were archived in the PACIFICA database (http://cdiac.ornl.gov/oceans/
188 PACIFICA/).

189

Marked Region	Cruise Name	Geographic Boundary	Date	Chief Scientist
East Sea				
1	CREAMS II	34.5°N –43.9°N 129.8°E–141.8°E	Jun–Jul 1999 Jul–Aug 1999	L. D. Talley (SIO, USA) V. Luchin (POI, Russia)
North Pacific Ocean				
2	P10	4.0°S–35.2°N 140.8°E–149.3°E	Oct–Nov 1993	M. Hall (WHOI, USA)
3	P13	4.7°S–54.2°N 161.1°E–165.4°E	Aug–Oct 1992	J. L. Bullister (PMEL, USA)
4	P14N	15.9°S–59.0°N 178.9°E–173.9°W	Jul–Sep 1993	G. I. Roden (UW, USA)
5	P16N	19.9°N–56.3°N 154.9°W–151.9°W	Feb–Apr 1991	J. L. Bullister (PMEL, USA)
6	P17N	34.5°N–57.3°N 159.0°W–123.8°W	May–Jun 1993	D. Musgrave (UA, USA)
	P17C	6.0°S–36.2°N 135.2°W–121.7°W	May–Jul 1991	M. Tsuchiya (SIO, USA)

190

Table S2.

Properties of end-member water masses included in the isopycnal analysis.

EM	PT (°C)	S	O_2 (μmol kg^{-1})	P (μmol kg^{-1})	N (μmol kg^{-1})	Si (μmol kg^{-1})	N^* (μmol kg^{-1})	*p*CFC-12 age (year)
Region 1 (East Sea)								
TMW	19.52 ± 0.01	34.50 ± 0.08	219.1 ± 10.5	0.17 ± 0.05	0.85 ± 0.32	2.90 ± 0.45	-1.9 ± 0.5	7.9 ± 0.8
ESIW	1.43 ± 0.05	34.04 ± 0.01	318.5 ± 14.9	0.91 ± 0.15	11.44 ± 2.12	16.80 ± 3.20	-3.5 ± 0.4	10.9 ± 1.3
ESPW	0.13 ± 0.01	34.07 ± 0.01	197.6 ± 4.9	2.12 ± 0.04	25.86 ± 0.22	89.40 ± 5.09	-7.0 ± 0.6	34.7 ± 1.0
Regions 2–6 (North Pacific Ocean)								
CCSW	12.44 ± 0.31	33.05 ± 0.02	269.8 ± 6.7	0.34 ± 0.06	0.32 ± 0.61	3.86 ± 0.28	-5.4 ± 0.4	2.6 ± 0.1
UNPCW	18.44 ± 0.30	34.86 ± 0.03	214.9 ± 16.5	0.18 ± 0.07	1.97 ± 1.23	3.16 ± 0.63	-0.8 ± 0.9	4.5 ± 2.8
LNPCW	7.67 ± 0.26	34.01 ± 0.03	206.2 ± 26.1	1.32 ± 0.21	19.97 ± 2.82	35.17 ± 7.03	-3.2 ± 1.6	15.1 ± 4.3

TMW: Tsushima Middle Water, ESIW: East Sea Intermediate Water, ESPW: East Sea Proper Water, CCSW: California Current System Water, UNPCW: Upper North Pacific Central Water, LNPCW: Lower North Pacific Central Water

References and Notes

1. R. A. Duce, J. LaRoche, K. Altieri, K. R. Arrigo, A. R. Baker, D. G. Capone, S. Cornell, F. Dentener, J. Galloway, R. S. Ganeshram, R. J. Geider, T. Jickells, M. M. Kuypers, R. Langlois, P. S. Liss, S. M. Liu, J. J. Middelburg, C. M. Moore, S. Nickovic, A. Oschlies, T. Pedersen, J. Prospero, R. Schlitzer, S. Seitzinger, L. L. Sorensen, M. Uematsu, O. Ulloa, M. Voss, B. Ward, L. Zamora, Impacts of atmospheric anthropogenic nitrogen on the open ocean. *Science* **320**, 893–897 (2008). Medline doi:10.1126/science.1150369

2. N. Gruber, in *Nitrogen in the Marine Environment, The Marine Nitrogen Cycle: Overview and Challenges*, D. G. Capone, D. A. Bronk, M. R. Mulholland, E. J. Carpenter, Eds. (Elsevier, Amsterdam, 2008), pp. 1–50.

3. T.-W. Kim, K. Lee, R. G. Najjar, H.-D. Jeong, H. J. Jeong, Increasing N abundance in the northwestern Pacific Ocean due to atmospheric nitrogen deposition. *Science* **334**, 505–509 (2011). Medline doi:10.1126/science.1206583

4. J. N. Galloway, Nitrogen mobilization in Asia. *Nutr. Cycl. Agroecosyst.* **57**, 1–12 (2000). doi:10.1023/A:1009832221034

5. G. S. Okin, A. R. Baker, I. Tegen, N. M. Mahowald, F. J. Dentener, R. A. Duce, J. N. Galloway, K. Hunter, M. Kanakidou, N. Kubilay, J. M. Prospero, M. Sarin, V. Surapipith, M. Uematsu, T. Zhu, Impacts of atmospheric nutrient deposition on marine productivity: Roles of nitrogen, phosphorus, and iron. *Global Biogeochem. Cycles* **25**, GB2022 (2011). doi:10.1029/2010GB003858

6. S. C. Doney, J. L. Bullister, A chlorofluorocarbon section in the eastern North Atlantic. *Deep-Sea Res. A* **39**, 1857–1883 (1992). doi:10.1016/0198-0149(92)90003-C

7. N. Gruber, J. L. Sarmiento, Global patterns of marine nitrogen fixation and denitrification. *Global Biogeochem. Cycles* **11**, 235–266 (1997). doi:10.1029/97GB00077

8. A. F. Michaels, D. Olson, J. L. Sarmiento, J. W. Ammerman, K. Fanning, R. Jahnke, A. H. Knap, F. Lipschultz, J. M. Prospero, Inputs, losses and transformation of nitrogen and phosphorus in the pelagic North Atlantic Ocean. *Biogeochemistry* **35**, 181–226 (1996). doi:10.1007/BF02179827

9. R. A. Fine, Observations of CFCs and SF_6 as ocean tracers. *Annu. Rev. Mar. Sci.* **3**, 173–195 (2011). Medline doi:10.1146/annurev.marine.010908.163933

10. A. Singh, M. W. Lomas, N. R. Bates, Revisiting N_2 fixation in the North Atlantic Ocean: Significance of deviations from the Redfield Ratio, atmospheric deposition and climate variability. *Deep-Sea Res. II* **93**, 148–158 (2013). doi:10.1016/j.dsr2.2013.04.008

11. A. C. Martiny, C. T. A. Pham, F. W. Primeau, J. A. Vrugt, J. K. Moore, S. A. Levin, M. W. Lomas, Strong latitudinal patterns in the elemental ratios of marine plankton and organic matter. *Nat. Geosci.* **6**, 279–283 (2013). doi:10.1038/ngeo1757

12. K. Lee, Global net community production estimated from the annual cycle of surface water total dissolved inorganic carbon. *Limnol. Oceanogr.* **46**, 1287–1297 (2001). doi:10.4319/lo.2001.46.6.1287

13. D. Karl, R. Letelier, L. Tupas, J. Dore, J. Christian, D. Hebel, The role of nitrogen fixation in biogeochemical cycling in the subtropical North Pacific Ocean. *Nature* **388**, 533–538 (1997). doi:10.1038/41474

14. H. Akimoto, H. Narita, Distribution of SO_2, NO_x and CO_2 emissions from fuel combustion and industrial activities in Asia with 1° × 1° resolution. *Atmos. Environ.* **28**, 213–225 (1994). doi:10.1016/1352-2310(94)90096-5

15. F. J. Dentener, Global maps of atmospheric nitrogen deposition, 1860, 1993, and 2050. Data set (Oak Ridge National Laboratory Distributed Active Archive Center, Oak Ridge, TN, 2006); http://daac.ornl.gov/.

16. J. Jung, H. Furutani, M. Uematsu, Atmospheric inorganic nitrogen in marine aerosol and precipitation and its deposition to the North and South Pacific Oceans. *J. Atmos. Chem.* **68**, 157–181 (2011). doi:10.1007/s10874-012-9218-5

17. J. H. Carrillo, M. G. Hastings, D. M. Sigman, B. J. Huebert, Atmospheric deposition of inorganic and organic nitrogen and base cations in Hawaii. *Global Biogeochem. Cycles* **16**, 1076 (2002). doi:10.1029/2002GB001892

18. J. M. Prospero, D. L. Savoie, R. Arimoto, Long-term record of nss-sulfate and nitrate in aerosols on Midway Island, 1981–2000: Evidence of increased (now decreasing?) anthropogenic emissions from Asia. *J. Geophys. Res.* **108**, 4019 (2003). doi:10.1029/2001JD001524

19. J. K. Moore, K. Lindsay, S. C. Doney, M. C. Long, K. Misumi, Marine ecosystem dynamics and biogeochemical cycling in the Community Earth System Model [CESM1(BGC)]: Comparison of the 1990s with the 2090s under the RCP4.5 and RCP8.5 Scenarios. *J. Clim.* **26**, 9291–9312 (2013). doi:10.1175/JCLI-D-12-00566.1

20. The 2% error is 1 SD from the mean export production estimated using the rate of seawater *N** increase found in regions 2 to 5 shown in Fig. 3.

21. K. Lee, D. M. Karl, R. Wanninkhof, J.-Z. Zhang, Global estimates of net carbon production in the nitrate-depleted tropical and subtropical oceans. *Geophys. Res. Lett.* **29**, 1907 (2002). doi:10.1029/2001GL014198

22. Future projections suggest that AND in 2030 may be up to 30% higher than in 2000 in the mid-latitude NPO (*1*). In particular, NH_x deposition in 2100 may be double that in 2000 (*24*), whereas NO_y deposition is likely to decrease substantially due to regulation of emissions. This perturbation, in conjunction with enhanced ocean stratification, could become a key factor determining future primary and export production in the NPO.

23. P. Suntharalingam, E. Buitenhuis, C. Le Quéré, F. Dentener, C. Nevison, J. H. Butler, H. W. Bange, G. Forster, Quantifying the impact of anthropogenic nitrogen deposition on oceanic nitrous oxide. *Geophys. Res. Lett.* **39**, L07605 (2012). doi:10.1029/2011GL050778

24. P. Ciais, C. Sabine, G. Bala, L. Bopp, V. Brovkin, J. Canadell, A. Chhabra, R. DeFries, J. Galloway, M. Heimann, C. Jones, C. Le Quéré, R. B. Myneni, S. Piao, P. Thornton, in *Climate Change 2013: The Physical Science Basis, Contribution of Working Group I to the Fifth Assessment Report of the Intergovernmental Panel on Climate Change*, T. F.

Stocker, D. Qin, G.-K. Plattner, M. Tignor, S. K. Allen, J. Boschung, A. Nauels, Y. Xia, V. Bex, P. M. Midgley, Eds. (Cambridge Univ. Press, Cambridge, 2013), chap. 6.

25. Mean wind data during 1990–1999 are available at www.esrl.noaa.gov/psd/.

26. M. Kanakidou, R. A. Duce, J. M. Prospero, A. R. Baker, C. Benitez-Nelson, F. J. Dentener, K. A. Hunter, P. S. Liss, N. Mahowald, G. S. Okin, M. Sarin, K. Tsigaridis, M. Uematsu, L. M. Zamora, T. Zhu, Atmospheric fluxes of organic N and P to the global ocean. *Global Biogeochem. Cycles* **26**, GB3026 (2012). doi:10.1029/2011GB004277

27. H. P. Hansen, F. Koroleff, in *Methods of Seawater Analysis: Determination of Nutrients*, K. Grasshoff, K. Kremling, M. Ehrhardt, Eds. (Wiley, Weinheim, Germany, 1999), pp. 159–228.

28. I.-N. Kim, D.-H. Min, D. H. Kim, T. Lee, Investigation of the physicochemical features and mixing of East/Japan Sea Intermediate Water: An isopycnal analysis approach. *J. Mar. Res.* **68**, 799–818 (2010). doi:10.1357/002224010796673849

29. L. D. Talley, G. L. Pickard, W. J. Emery, J. H. Swift, *Descriptive Physical Oceanography: An Introduction* (Elsevier, Boston, 2011).

30. R. Poole, M. Tomczak, Optimum multiparameter analysis of the water mass structure in the Atlantic Ocean thermocline. *Deep-Sea Res. I* **46**, 1895–1921 (1999). doi:10.1016/S0967-0637(99)00025-4

31. M. Tomczak, D. G. B. Large, Optimum multiparameter analysis of mixing in the thermocline of the eastern Indian Ocean. *J. Geophys. Res.* **94**, 16141–16149 (1989). doi:10.1029/JC094iC11p16141

32. J.-F. Lamarque, F. Dentener, J. McConnell, C.-U. Ro, M. Shaw, R. Vet, D. Bergmann, P. Cameron-Smith, S. Dalsoren, R. Doherty, G. Faluvegi, S. J. Ghan, B. Josse, Y. H. Lee, I. A. MacKenzie, D. Plummer, D. T. Shindell, R. B. Skeie, D. S. Stevenson, S. Strode, G. Zeng, M. Curran, D. Dahl-Jensen, S. Das, D. Fritzsche, M. Nolan, Multi-model mean nitrogen and sulfur deposition from the Atmospheric Chemistry and Climate Model Intercomparison Project (ACCMIP): Evaluation of historical and projected future changes. *Atmos. Chem. Phys.* **13**, 7997–8018 (2013). doi:10.5194/acp-13-7997-2013

33. J. M. Prospero, D. L. Savoie, Effect of continental sources on nitrate concentrations over the Pacific Ocean. *Nature* **339**, 687–689 (1989). doi:10.1038/339687a0